J. Indian Inst Sci., Nov.–Dec 1999, **79**, 551–584.

IISc THESES ABSTRACTS

Thesis Abstract (Ph. D.)

Structural and thermodynamic studies on protein stability by Balasubramanian Gopal
Research supervisor: Prof. M. R. N. Murthy
Department: Molecular Biophysics Unit

1. Introduction

Proteins are the products of gene sequence. Their form and function depend on their amino-acid sequence. The three-dimensional structure of a protein concurrent with its local concentration and spatial location determines its role in a biological system. The study of proteins encompasses three broad areas:

(i) The translation of an amino-acid sequence into a three-dimensional structure.
(ii) The dependence of function/activity on this structure.
(iii) The modulation of function in the interests of its biochemical action.

The investigations reported in this work include:

a. Structural and biophysical characterization of a calcium-binding protein (CaBP) from the parasitic ameboid *Entamoeba histolytica.*
b. Investigations on the structural effects of site-specific mutations in the dimeric interface of Thymidylate Synthase (TS) from *Lactobacillus casei* and Triosephosphate Isomerase (TIM) from *Plasmodium falciparum.*

2. Results and discussion

CaBP is a highly soluble, monomeric protein (14.7 kd) without disulfides or *cis*-prolyl peptide bonds. It binds calcium (4 ions per monomer) and both the holo and apo forms of the protein are thermostable. CaBP has, therefore, been used as a model system to carry out studies on protein structure and stability.

The thermodynamics of the binding of calcium and magnesium ions to CaBP was investigated by isothermal titration calorimetry (ITC) in 20 mM MOPS buffer (pH 7.0) at 20°C[1]. Enthalpy titration curves of calcium show the presence of four Ca^{2+}-binding sites. There exist two low-affinity sites for Ca^{2+}, both of which are exothermic in nature and with positive cooperative interaction between them. Two other high-affinity sites for Ca^{2+} include one endothermic and the other exothermic, again with positive cooperative interaction. The binding constant for Ca^{2+} at the four sites has been verified by a competitive binding assay, where CaBP competes with a chromophoric chelator 5, 5' Br_2 BAPTA to bind Ca^{2+}. The enthalpy of titration of magnesium in the absence of calcium is single state and endothermic in nature. In the case of titrations performed using protein pre-saturated with magnesium, the amount of heat produced is altered. Further, the interaction between the high-affinity sites changes to negative cooperativity. No absorption of heat was observed throughout the addition of magnesium in the presence of 1 mM calcium. Titrations performed on a cleaved peptide comprising the N-terminus and the central linker show the existence of two Ca^{2+}-specific sites. These results indicate that this CaBP has one high-affinity Ca^{2+}-Mg^{2+} site, one high-affinity Ca^{2+}-specific site and two low-affinity Ca^{2+}-specific sites.

The thermodynamic parameters of the binding of these metal ions were used to elucidate the energetics at the individual site(s) and the interactions involved therein at various concentrations of the denaturant, guanidine hydrochloride (GdnHCl) ranging from 0.05 to 6.5 m.[1] Unfolding of the protein was also monitored by titration calorimetry as a function of the concentration of the denaturant. These data show that at a GdnHCl concentration of 0.25 M, the binding affinity for the Mg^{2+} ion is lost and there are only two sites which can bind to Ca^{2+}, with substantial loss of cooperativity. At concentrations beyond 2.5-M GdnHCl, at which the unfolding of the tertiary structure of this protein is observed by near UV CD spectroscopy, the binding of Ca^{2+} ions is lost. We thus show that the domain containing the two low-affinity sites is the first to unfold in the presence of GdnHCl. Control experiments with change in ionic strength by the addition of KCl in the range of 0.25 to 1M show the existence of four sites with altered ion-binding parameters.

Equilibrium denaturation studies on both the apo and holo forms of this protein indicate the presence of stable transition intermediates at low denaturant concentrations which exhibit an ability to bind to the non-specific hydrophobic dye ANS.[2] The hydrodynamic properties of these intermediates have been further examined using size-exclusion chromatography. The association and dissociation rates of metal ion-binding as well as denaturation in the presence of the GdnHCl for native protein in the apo and holo forms have been characterized by stopped flow kinetics, employing the intrinsic tyrosine fluorescence of this protein. Furthermore, the preferential binding of Gdn^+ ions to the cation-binding sites in the N-terminal domain and its influence on the behavior of the EF hand sites on the C-terminal domain have been examined using ITC.

CaBP was crystallized using the hanging drop method with 2-methylpentan 2-4-diol (MPD) as the precipitant.[3] X-ray diffraction data have been collected on these crystals using an MAR imaging plate detector system attached to a Rigaku RU200 rotating anode X-ray generator. The crystals belong to the hexagonal space group $P6_122$ with unit cell dimension of $a = b = 96.21$ Å, $c = 65.48$ Å. Preliminary molecular replacement computations suggest that the structure of this protein is likely to be similar to that of Calmodulin (CAM), the notable difference being the relative orientation of the two domains.

Studies on the interface mutants of TS and TIM were carried out with a view to understand the structural determinants of dimer stability. Three mutants, two of TS (R178F and R218K) and one of TIM (Y74C), were examined. The crystal structures of the R178F mutant of TS and the Y74C mutant of TIM were determined. The R218K mutant of TS failed to crystallize.

The significance of two interface residues in the structural integrity of the TS dimeric state was investigated by thermal and chemical denaturation.[4] While R178F mutant showed apparent stability to thermal denaturation by its decreased tendency to aggregate, the R218K mutant was destabilized by 5°C. Crystallographic analysis of R178F reveals no obvious change as a consequence of amino-acid substitution. An attempt has been made to rationalize the results in terms of mutational effects on the folded and unfolded state of the molecule. Evidence is provided for the utility of site-specific amino-acid substitutions in identifying regions of TS involved in non-native protein association. These results may have general implications for mutational studies on multisubunit proteins.

The phenomena of unit cell transformation upon radiation exposure in TS crystals was examined using crystals of the R178F mutant.[5] Some crystal forms of TS exhibit unit cell transformation upon exposure to X-ray radiation. These forms, all of which occur in the space group $P6_122$, show an elongation in the 'c' cell dimension, which in some cases stabilize to a constant cell dimension upon prolonged exposure. We present here an analysis of the possible causes of this transformation based on the crystal structures that we have obtained for two crystal forms of the R178F mutant of this enzyme. These structures have been compared with crystal structures having intermediate cell dimensions reported in the literature. We present differences in the crystal structures of transformed and untransformed forms. The transformation appears to occur by a concerted change in the packaging of molecules in the unit cell and minor changes in regions of the molecule which participate in the intersubunit contacts.

The crystal structure of the Y74C mutant of TIM[6] helps to analyse the effects of crosslinking mutations in the protein interface in the case of multimeric proteins. An intersubunit disulfide bridge was introduced across the interface of the dimeric enzyme. This was achieved by mutating a tyrosine residue at position 74 to a cysteine thereby enabling it to form a covalent crosslink with a native cysteine at position 13 of the other monomer. The *bis*-oxidized form of the mutant was found to be less active than the native enzyme, but had similar stability as that of the wild type. The reduced form of the mutant was much less stable. The crystal structure of the mutant offers insights into the role of the interfacial cavities and the role of disulfide tethering in restoring protein stability.

References

1. GOPAL, B *et al.* Thermodynamics of metal ion binding and denaturation of a calcium binding protein from *Entamoeba histolytica*, *Biochemistry*, 1997, **36**, 10910–10917.
2. GOPAL, R. *et al.* Induction of a spectrascopically defined transition by guanidium hydrochloride on a recombinant calcium binding protein from *Entamoeba histolytica*, *FEBS Lett.*, 1998, **441**, 71–76..
3. GOPAL, B. *et al.* Crystallization and preliminary X-ray studies of a recombinant calcium binding protein from *Entamoeba histolytica*, *Acta Cryst. D*, 1998, **54**, 1442–1445.
4. PRASANNA, V. *et al.* Effect of amino acid substitutions at the subunit interface on the stability and aggregation properties of a dimeric protein: critical role of arginine at the dimer interface of thymidylate synthase, *Proteins*, 1994, **34**, 356–368.
5. GOPAL, B. *et al.* Crystals of a thymidylate synthase mutant offer insights into crystal packing and protein plasticity, *Curr. Sci.*, 1998, **75**, 299–304.
6. GOPAL, B. *et al.* Cavity creating mutation at the dimer interface in *Plasmodium falciparum* triosephosphate isomerase: Restoring protein stability by disulfide crosslinking of subunits, *Biochemistry*, 1998, **31**, 478–486.

Thesis Abstract (Ph. D.)

Studies on the nonstructural proteins NS2B and NS3 of Japanese encephalitis virus–Indian strain P20778 by Yuvarani S. Kuppumbatti
Research supervisor: Prof. A. Antony
Department: Microbiology and Cell Biology

1. Introduction

Japanese encephalitis virus (JEV) is a positive-stranded RNA virus that belongs to the family *Flaviviridae* and genus flaviviruses. The genus flaviviruses includes more than 68 members separated into groups on the basis of serological relatedness. Flaviviruses cause serious health diseases both in humans and animals. The majority are arthropod-borne and are transmitted to vertebrates by chroically infected mosquito or tick vectors. The genome of JEV is approximately 11-kb long. The genomic RNA is infectious and encodes the viral proteins necessary for RNA replication. In virus-infected cells, the genomic RNA is translated into a polyprotein of approximately 350 kDa. The order of protein encoded in 5' and C-PrM-E-NSI-NS2A-NS2B-NS3-NS4A-NS4B-NS5 3'. The polyprotein is processes to individual proteins by both host-cell signalase and viral protease.

The work presented here focuses on the nonstructural proteins NS2B and NS3 of Indian strain P20778 of JEV. The present study describes (1) sequencing and the sequence analysis of the NS3 gene, (2) cloning and expression of the NS3 gene, (3) cloning and expression of the NS2B gene and (4) the activity of the protease.

2. Experimental

Cloning and subcloning were performed according to the methods described by Sambrook *et al.*[1] DNA sequence of the NS3 gene was determined using Sangers dideoxy chain termination method.[2] Polymerase chain reaction was performed according to the method of Saiki and co-workers.[3] The proteins expressed in *E. coli* was analysed by SDS-PAGE and Western blotting technique.[4] N-terminal protein sequencing was carried out using automated gas-phase sequenator model PSQ-1 from Shimadzu.

3. Results and discussion

The complete nucleotide sequence of the NS3 gene of P20778 was determined. The NS3 gene is 1857 nucleotides along and encodes NS3 protein of 619 amino acids. Comparison of the nucleotide sequence of P20778 with the NS3 gene of Japanese strain JaoArS982 reveals 95.9% homology. Restriction enzyme site analysis of P20778 and JaoArS982 reveals the appearance of eight new sites (Asu II, Ava I, Bgl II, NheI, two Msc I, Sac I, Pst I) and disappearance of five sites (Acc I, two Bbv II, Hgi AI, Tth IIII) in P20778.

Comparison of deduced amino-acid sequence of P20778 with the NS3 gene of JaoArS982 shows 98.38% homology. A few notable amino-acid changes occurred in P20778 at positions 398, 402 and 467. At position 398, lys (K) was replaced by glu (E). At position 402 asp (D) was replaced by ala (A), where a negatively charged amino acid was converted to a nonpolar amino acid. At position 467, a polar uncharged amino acid asn (N) was replaced by the positively charged amino acid lys (K). The pI of NS3 protein of P20778 and JaoArS982 was calculated to be 7.32 and 7.12, respectively.

The N-terminal 184 amino acids of NS3 (P20778) revealed significant homology with cellular proteases in the four regions of NS3. H_{51}, D_{75}, and S_{135} comprise the catalytic triad of NS3 protease. The conserved motif G-X-S-G-X-P present in the NS3 of P20778 and other flaviviruses represents the sequence surrounding the serine protease nucleophilic serine. The conserved D_{129} residue followed by either Y, F, or L and the conserved motif G-L-Y-G-N-G are hypothesized to form part of the substrate-binding pocket which partially determines the cleavage specificity.

The NS3 gene of P20778 was cloned into the T7 promoter-based vector pET3d. The recombinant construct was proved to be nonproductive due to the presence of a stem-and-loop structure comprising nucleotides from 3-30 of the coding sequence of NS3 mRNA, whose free energy was calculated to be –13.4 kcal/mol. The protease activity of NS3 protein was shown to be present within the N-terminal 184 amino acids in flaviviruses. The amino acids coded by the stem-and-loop structure may be required for proper folding and protease activity. A novel strategy was employed to overcome the inhibition of translation initiation in the NS3 gene. It has been reported that the translating ribosomes were capable of unfolding RNA secondary structures and the energy required may be derived from the hydrolysis of GTP which drives the protein synthesis. A new set of primers was designed to provide: i) a new start codon upstream of the one involved in the secondary structure; ii) a distance of 12 nucleotides between the new start codon and the stem-and-loop structure which provides the stretch of mRNA occupied by the ribosome in the initiation complex; and iii) a second codon for flycine, which is required to facilitate the removal of the initiator 'methionine'. The NS3 gene was cloned and expressed in T7 promoter-based vector pET3d using the new set of primers.

The initiation of NS3 gene expression at the upstream AUG was confirmed by protein sequencing. The deletion of the stem-and-loop structure in the nonproductive construct led to the expression of the truncated NS3 gene, which proves that the presence of this structure inhibited NS3 gene expression. The presence of NS3-specific mRNA in *E. coli* cells harboring both the productive and the nonproductive constructs was confirmed by Northern blot analysis. The protease domain of NS3 gene was expressed in pET3d vector and the authenticity of this protein (NS3T) was confirmed by Western blotting.

NS2B, another virus-encoded nonstructural protein, is required for the proteolytic activity of the NS3 protein. In order to study the proteolytic function of NS3 protein, expression of the NS2B gene is obligatory. The NS2B gene was expressed as GST–NS2B fusion protein in the vector pET3d. The protein was affinity purified using the glutathione–agarose affinity matrix. During subsequent transformations and inductions, only GST protein was obtained. The NS2B gene was expressed as NS3T–NS2B fusion protein which can be used in protease assay *in vitro*.

A fluorogenic peptide substrate Dns–NKKRGWPA for NS3T-NS2B protease was synthesized using Fmoc solid-phase peptide synthesis. The NS3T-NS2B protein was found to be in the inclusion body. *E. coli* cells harboring the recombinant plasmid were grown in M9 medium either at 20°C or 30°C. The protein obtained under these conditions was found to be in insoluble form. The inclusion body protein was isolated, partially purified and solubilized in 8 M urea/6 M guanidinium hydochloride. Attempts to refold the protein using different methods like stepwise dialysis, stepwise dilution and dialysis in *tris* buffer with or without glutathione redox system did not yield the active enzyme.

An alternate strategy was employed to demonstrate the proteolytic activity of the NS3T–NS2B protease, using a recombinant plasmid that codes for both the enzyme and substrate. The recombinant plasmid codes for the polyprotein NS3T–NS2A–NS2B, where NS3T is the protease domain of NS3 and NS2B is the activator. The natural cleavate site between NS2A and NS2B was provided as the substrate. The recombinant plasmid, upon induction with IPTG, synthesizes the polyprotein, which undergoes self cleavage and yields the cleavage product 47 kDa protein.

In conclusion, the complete nucleotide sequence of the NS3 gene of P20778 was determined and the length of the gene was found to be 1857 nucleotides. NS3 consensus-region primers may be used for JEV detection by RT-PCR. The novel expression strategy used in this study can be applied to express other genes in which a stem-and-loop structure is involved in the inhibition of translation initiation. This strategy is tested and validated by the demonstration of the proteolytic activity of the P20778 protease. This study demonstrated for the first time the activity of bacterially expressed JEV protease.

References

1. Sambrook, J., Fritsch, E. F. and Manitis, T. *Molecular cloning. A laboratory manual*, 2nd edition, Cold Spring Harbor Laboratory, Cold Spring Harbor, New York, 1989.
2. Sanger F., Nickles, S. and Coulson, A. R. *Proc. Natn. Acad. Sci. USA*, 1977, **74**, 5463–5467.
3. Saiki, R. K. *et al* *Science*, 1985, **230**, 1350–1354.
4. Towbin, H., Staehelin, T. and Gorden, J. *Proc. Natn. Acad. Sci. USA*, 1979, **76**, 4350–4354.

Thesis Abstract (M. Sc. (Engng))

Fine ceramic pigments: Combustion synthesis and properties by Samrat Ghosh
Research supervisors: Profs K. C. Patil and K. Kishore
Department: Inorganic and Physical Chemistry

1. Introduction

Ceramic pigments are coloured inorganic metal oxides. They are industrially important due to widespread application for aesthetic enhancement in dinnerware, sanitaryware, tiles, porcelain enamels, high-temperature artware and structural clay products. For successful application of ceramic pigments in industry, they should be a) homogeneous in colour and have high tinctorial strength, b) fine (1–10 μm) and possess high surface area, c) stable under reducing, corrosive and thermal conditions (> 1100 °C), d) cost effective, and e) nontoxic. Colour making is a specialized field of ceramics. It involves extensive and intensive research and development on the part of the producer as many of the processes are patented. In India, there is still not much concerted effort on R&D on ceramic pigments. The solid-state preparative method employed by the industry for the ceramic pigments usually requires high temperature (1000–1400°C), long processing time (several hours to days) and use of mineralizers to facilitate the reaction. The end products are usually coarse, compositionally inhomogeneous and as such are unsuitable for application. They require further processing to produce fine powders. Thus, the conventional ceramic method of preparation of fine ceramic pigaments is tedious, energy-intensive, time-consuming and expensive. Over and above, due to strict environmental legislation, some pigments and processes currently in use are on the verge of being phased out. Furthermore, scarcity and consequent high price of transition metal compounds like those of cobalt have made its pigment cost prohibitive. So the use of such compounds has to be optimized. Hence, there is considerable incentive to explore alternative routes which would be shorter, low-temperature initiated, simple, cost-effective and nonvitiating for the synthesis of fine ceramic pigments. Low-temperature chemical methods (Chimie Douce) have been developed to overcome these limitations of the conventional solid-state method. These include sol–gel,[1] coprecipitation,[2] aerosol hydrolysis[3] etc. These synthetic methods are quite intricate, require long processing times, costly chemicals and elaborate experimental set-up.

Muthuraman *et al.*[4] have employed novel solution combustion method to synthesize zirconia-based fine pigments. It is essentially a low-temperature initiated, self-propagating, gas producing, exothermic redox reaction involving metal nitrates and an organic fuel like urea. The utility of the technique has already been demonstrated in the synthesis of a variety of high surface area, fine oxides ranging from alumina to zirconia.[5] The present study aims at the synthesis of some industrially important fine ceramic pigments based on alumina, aluminates, borates, ceria, chromites, silicates and zirconia by novel combustion process, investigate their particulate properties like agglomerate size, surface area, etc., investigate the effect of processing parameters like nature of fuel, precursors and extra oxidizers on the colour and particulate properties of combustion-derived ceramic pigments and to correlate the colours of cobalt (II) ceramic pigments and the coordination compounds of cobalt (II) ions in solution.

2. Experimental

The set-up for combustion synthesis involves a combustion chamber which is an electric furnace operating on 240V AC–13.75 amp current. Chrome–alumina thermocouple was used to measure the furnace temperature. A medium-sized exhaust fan for venting the fumes emanating from the combustion process was positioned such that the convection current does not affect the combustion process. The temperature of the flame which appears during the combustion process was measured using an optical pyrometer.

The various hydrazine-based fuels used for the combustion synthesis of ceramic pigments were carbohydrazide (CH), N, N'-diformylhydrazine (DFH), oxalyldihydrazide (ODH) and tetraformaltrisazine (TFTA). These fuels were prepared in the laboratory according to procedures describe elsewhere.[6–9] The fuel, urea, used was of laboratory grade.

3. Calculation of the stoichiometry of redox mixtures

The stoichiometry of redox mixtures used for combustion were calculated using the total oxidizing and reducing valencies of the components which serve as numerical coefficients for the stoichiometric balance so that the equivalence ratio (ϕ_e) is unity and the energy released by combustion is maximum and without any carbon residue.[10] According to this concept, the valence of $C = +4$, $H = +1$, divalent metal ions = +2, trivalent metal ions = +3 and so on, and $O = -2$. The valence of nitrogen is considered to be zero. Based on these considerations, aluminium nitrate will have an oxidizing valence of –15, and urea a reducing valence of +6. The mole ratio of aluminium nitrate:urea required for the preparation of alumina becomes 1:2.5.

3.1. *Combustion synthesis of 1 atom % Co^{2+}: α–Al_2O_3*[11]

A petri dish (300 cm^3) containing 20 g of $Al(NO_3)_3.9H_2O$, 8 g urea and 0.15 g of $Co(NO_3)_2.6H_2O$ was introduced into a muffle furnace preheated to 500 °C. The mixture initially melts in the water of hydration of the aluminium nitrate. This solution boils, dehydrates with the formation of a gel. This gel foams and catches fire, which smoothly glows to incandescence (flame temperature ~ 1500°C) yielding a voluminuous blue coloured product. In order to study the effect of various fuels, other blue alumina pigments Co^{2+}: MAl_2O_4, where M is Mg, Zn, were prepared from corresponding metal nitrates–urea/ODH/DFH fuel. Cobalt- and nickel-doped hexaaluminates, Co^{2+}/Ni^{2+}: $MAl_{12}O_{19}$, where M is Ca, Sr, were prepared by combustion of aqueous solution containing different calcium salts (acetate, carbonate), aluminium nitrate and urea redox mixtures. $CoAl_2O_4/NiAl_2O_4$ pigments were prepared using both ODH and CH fuels. Chrome pink alumina pigments prepared by combustion of stoichiometric amounts of corresponding metal nitrates and appropriate fuel are: Cr^{3+}: αAl_2O_3 (urea), Cr^{3+}: MAl_2O_4, where M is Mg, Zn and Cr^{3+}: $Y_3Al_5O_{12}$ (CH). Highly voluminous (foam density = 0.004 g/cc) fine pink coloured 1 atom % Cr^{3+}: α-Al_2O_3 was obtained from redox mixture containing aluminium nitrate, urea, zinc acetate and chromium acetate. The various borate pigments synthesized by using carbohydrazide fuel are: rose pink (Co^{2+}: $Mg_2B_2O_5$),[11] violet (Co^{2+}: ZnB_4O_7), purple ($Co_2B_2O_5$) and lemon green ($Ni_3B_2O_6$). Praseodymium-doped red ceria pigments (Pr^{4+}: CeO_2) were synthesized using both redox compound, $Ce_{1-x}Pr_x(N_2H_3COO)_3.3H_2O$ and redox mixture containing corresponding metal nitrates and ODH/TFTA fuels. Olive-green $NiCr_2O_4$ and peacock-green $CoCr_2O_4$ were prepared from redox mixtures containing corresponding metal nitrates—urea, ODH, TFTA fuels. 1 atom % Co^{2+}: Zn_2SiO_4 a lavender-coloured pigment was prepared from a redox mixture containing stoichiometric amounts of metal nitrates, fumed silica (210 m^2/g), DFH and NH_4ClO_4 as additional oxidizer. The various zincite pigments synthesized from metal nitrates, ODH/TFTA redox mixtures are Co^{2+}: ZnO (green), Mn^{2+}: ZnO (yellow), Ni^{2+}: ZnO (mustard green) and Fe^{3+}: ZnO (orange). Praseodymium- and vanadium-doped yellow zirconia pigments were prepared by combustion of redox mixture containing stoichiometric amounts of zirconyl nitrate, CH, ammonium vanadate/praseodymium nitrate in the molar ratio 4:5:0.04. Zirconyl nitrate was prepared by dissolving zirconium carbonate in dilute HNO_3.

4. Results and discussion

Low-temperature initiated, self-propagating, gas-producing, combustion process yields homogeneously coloured ceramic pigments. This is due to uniform doping of colorants in the oxide host. In cobalt blue alumina, zinc orthosilicate and zincite pigments, Co^{2+} is in the tetrahedral site whereas in rose pink, (Co^{2+}: $Mg_2B_2O_5$) pigment occupies octahedral site. In chrome pink alumina pigments, Cr^{3+} substitutes for Al^{3+} in the octahedral site. The combustion-derived pigments are X-ray crystalline, voluminous (foam density = 0.005–0.02 g/cc), sub-micron-sized pigments with large surface area (5-85 m^2/g). The fine particulate nature of the combustion-derived pigments is reflected in their average crystallite size (8-40 nm) and agglomerate size (0.95–10 μm). The powder densities (50–80% of the theoretical density) indicate the fluffy nature of the combustion-derived pigments. Actually one needs smaller amounts of these fine ceramic pigments than the coarse pigments prepared by the solid-state reaction to coat a given surface of the ceramic body. The combustion-derived pigments are fuel specific. Urea is an ideal fuel for the synthesis of alumina pigments. Borate and silicate pigments could be synthesized by using only CH and DFH fuels, respectively. Zincite pigments could be synthesized using ODH or TFTA. Dark-green Co^{2+}: ZnO was obtained using TFTA, whereas ODH yielded a lighter shade. Amorphous coral-coloured Pr^{4+}: CeO_2 was obtained with ODH, whereas TFTA yielded an X-ray crystalline brick-red product. This is attributed to the highly exothermic combustion with TFTA compared to ODH. $NiAl_2O_4$ obtained using CH had a lighter shade and higher surface area (85 m^2/g) compared to that obtained using ODH (12 m^2/g). Similar observation was made when metal acetate precursor was used in lieu of metal nitrates. The surface area of Co^{2+}: $CaO.6Al_2O_3$ obtained using calcium acetate was 12 m^2/g compared to that obtained using nitrate precursor (8 m^2/g). Similarly, chromium acetate and zinc acetate yielded a bright pink Cr^{3+}: α Al_2O_3 with surface area of 16 m^2/g which is almost twice that obtained using chromium nitrate.

Hence the novel solution combustion method is a unique synthetic route to fine ceramic pigments. Unlike conventional ceramic method, the present method is fast, low-temperature initiated, instantaneous, obviates use of mineralizers and requires no elaborate set-up. Being a solution process, homogeneity, purity and molecular-level doping of colorants in the inorganic oxide matrices are achieved.

References

1. Monros, G., Carda, J. and Alarcon, J. *Br. Ceram. Trans. J.*, 1991, **90**, 157–160
2. Stefani, R. and Longo, E. *Am. Ceram. Soc. Bull.*, 1997, **76**, 61–65.
3. Pedro Tartaj, Serna, C. J. and Nanuel Ocana *J. Am. Ceram. Soc.*, 1995, 1147–1151
4. Muthuraman, M., Arul Dhas, N. and Patil, K. C. *J. Mater. Synth. Processing*, 1996, 4, 115–118.
5. Patil, K. C. Aruna, S. T. and Ekambaram, S. *Curr. Opinion Solid St Mater. Sci.*, 1997, **2**, 158–165
6. Mohr, E B., Brezenski, J. J and Andrieth, L F. *Inorg Synth.*, 1953, **4**, 32–34
7. Ainsworth, C. and Jones, R. G. *J. Am. Chem. Soc.*, 1955, **77**, 621–624.
8. Gran, G. *Anal. Chem. Acta*, 1956, **14**, 150–153.
9. Mashima, M. *Bull. Chem. Soc. Jap*, 1996, **39**, 504–507.
10. Jain, S. R., Adiga, K. C and Pai Verneker, V. R *Combust. Flame*, 1981, **40**, 71–76.
11. Patil, K. C., Ghosh, S., Aruna, S. T. Ekambaram, S. *Indian Potter*, 1996, **34**, 1–9.

Thesis Abstract (Ph. D.)

Guanylyl cyclase C receptor: A model system to study biomolecular interactions by Animesh Nandi

Research supervisor: Prof. Sandhya Visweswaraiah
Department: Molecular Reproduction Development and Genetics

1. Introduction

Cyclic guanosine monophosphate (cGMP) acts as intracellular second messenger in response to a variety of endo- and exogenous stimuli. Cyclic GMP is generated intracellularly by enzymes called guanylyl cyclases which cyclize the magnesium-bound GTP substrate to 3'5' cGMP. These enzymes can be isolated from both the cytosol and membrane fractions of cells. The cytosolic forms are heterodimers and activated by nitric oxide,[1] whereas the membrane-bound forms are peptide-stimulatable receptors of a single polypeptide chain.[2, 3] The domain organization of the membrane-associated guanylyl cyclases include a large extracellular ligand-binding domain, a short transmembrane domain, a protein kinase-like domain and a cyclase domain.[3] Many isoforms of the membrane associated, receptor guanylyl cyclases have been cloned and named GCA, GCB, GCC, GCD, GCE, GCF. A number of peptide ligands have been isolated which bind particulate guanylyl cyclases. The peptides which bind GCA and GCB receptors are natriuretic peptides. The heat-stable enterotoxins (STs), guanylin and uroguanylin peptides bind to GCC.[4] GCD, GCE and GCF are still orphan receptors.

The ability of guanylyl cyclase C (GCC) to bind a variety of stable toxin peptides and endogenous peptides like guanylin and uroguanylin makes it an ideal candidate for the study of molecular interactions. Antibodies to GCC can in addition contribute substantially to the understanding of ligand–receptor interactions. Also expression of GCC in malignant extraintestinal tissues makes it an interesting subject for metastatic colon cancer studies.

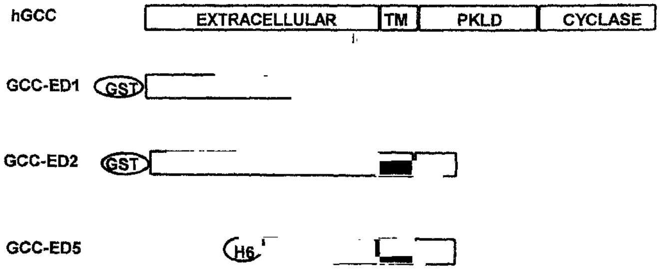

FIG. 1. Schematic representation of the structure of various domains of GCC: TM–Transmembrane domain; PKLD–Protein kinase-like domain; GCC-ED–Guanylyl cyclase C extracellular domain; GCC-ID-Guanylyl cyclase C intracellular domain; GST-Glutathione S-transferase; H6-Hexahistidine tag.

2. Experimental results and discussion

In order to study the role of the large extracellular domain of GCC which binds the ST peptides, guanylin and uroguanylin with tremendous specificity and to raise antibodies to the receptor, various domains of the human receptor were cloned as fusion proteins and expressed in *E. coli*. The extracellular domain was cloned as fusion proteins to glutathione S-transferase (Fig. 1) and the proteins were called GCC-EDI and GCC-ED2. GCC-ED1 comprises the N-terminal region of the receptor and has an Mr of 57 kDa, whereas GCC-ED2 is a protein of 81 kDa and encompasses the complete extracellular domain, the transmembrane domain and a short stretch of 63 amino acids of the intracellular domain. These proteins were initially

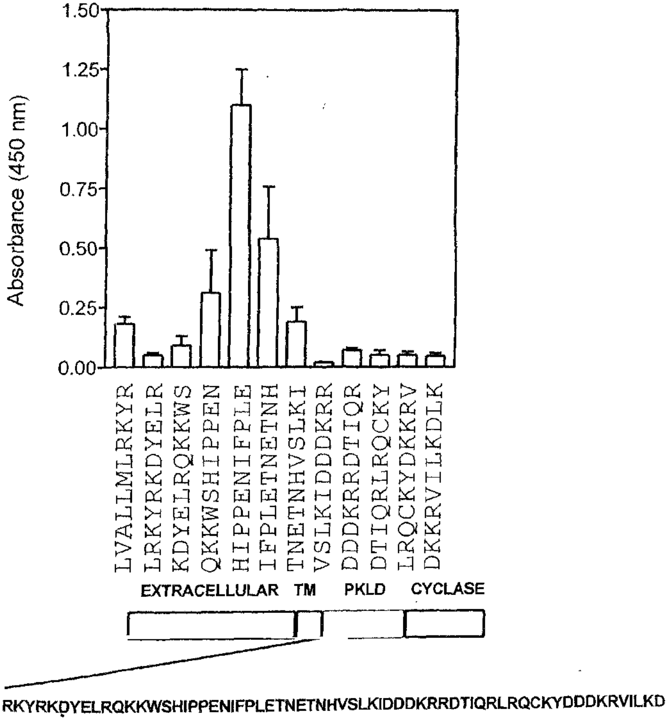

FIG 2. Epitope mapping of GCC:B10 monoclonal antibody using peptides synthesised on polyethylene pins.

purified from inclusion bodies by electroelution and were used to generate antibodies. However, to retain the protein in the soluble state, growth and induction temperature of *E. coli* cells were lowered to 16°C. Also the pellet was subjected to detergent extraction prior to glutathione affinity purification. The affinity-purified protein, GCC-ED2, was active and bound STh ligand with an affinity similar to that of the native, full-length, glycosylated, post-translationally modified receptor present in intestinal cells. It also displayed increased binding to ST peptides at lower pHs similar to the receptor purified from intestinal cells. However, under similar conditions, GCC-ED1 protein did not show any binding activity; hence, it can be suggested that the complete sequence of the amino acids corresponding to the extracellular domain are required for high-affinity interaction.[5] Antibodies were raised to GST fusion proteins and affinity selected against GST. These receptor-specific antibodies recognized GCC in the human T84 colonic cell line by Western blots and were able to inhibit ST binding and subsequent signalling events. Since inhibition was observed with antibodies raised against all fragments of the receptor, it can be hypothesized that ligand-binding regions are distributed throughout the extracellular domain of GCC. This result is in full agreement with our earlier finding that the complete extracellular domain of GCC is involved in ligand binding. Also, these critical regions are conserved in the rat receptor because the antibodies to the human receptor were able to neutralize binding to the rat receptor.[5]

In order to investigate the cellular localization of GCC, the generation of a GCC-specific monoclonal antibody was envisaged. The unique domain in GCC, distinct from other members of the guanylyl cyclase family allowed the use of only the extracellular domain for GCC-specific antibody production. GCC-ED2 protein was used as an antigen to generate a monoclonal antibody designated GCC : B10. The antibody recognized the receptor in Western blots with membranes prepared from T84 cells.[6] The epitope for the monoclonal antibody was iden-

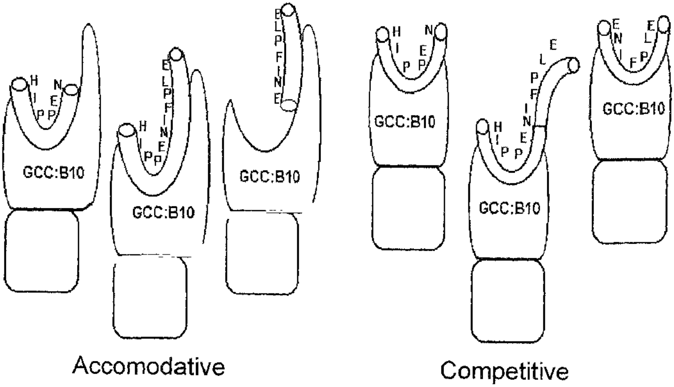

FIG. 3. Proposed model for the interaction of the peptides HIPPEN, ENIFPLE and HIPPENIFPLE.

tified using various extracellular and intracellular domain constructs expressed in *E. coli* (Fig. 1) and peptide synthesis. Maximum reactivity of the monoclonal antibody was detected with the peptide sequence HIPPENIFPLE which is located 15 amino acids distal to the transmembrane domain (Fig. 2). This sequence was unique to GCC and not present in other guanylyl cyclase isoforms.[7] The IC_{50} of interaction of the peptide with the monoclonal antibody was determined to be 2×10^{-7} M.

GCC was localised immunohistochemically using GCC : B10 monoclonal antibody to the columnar epithelial cells of rat intestinal sections. No staining was observed in any other strata of the intestine.

Expression was uniform throughout the villus-to-crypt axis of the small intestine similar to G-Kinase II expression. However, in the large intestine the expression was restricted to the crypt cells similar to that reported for cystic fibrosis transmembrane conductance regulator (CFTR) expression. Therefore, additional downstream effectors of GCC/cGMP signalling can be suggested.[6]

To identify the core epitope and the sequences involved in epitope recognition phage display technology was used, and GCC : B10 was panned with a random pentavalent hexameric phage display library constructed in the pIII coat protein of fd-tet bacteriophage. Two classes of phage sequences were obtained and these were different from the native peptide sequence used to elute the phages. However, based on the proline residues these phages could be aligned at two different positions in the HIPPENIFPLE sequence suggesting the possibility of two independent sites in the native receptor sequence that could interact with GCC : B10. This was confirmed by antibody reactivity with peptides corresponding to the two sites, namely, HIPPEN and ENIFPLE. Also each of the two peptides were able compete the binding of the other peptide as well as the full-length peptide suggesting that each peptide defines an epitope independent of the other and are mimotopes of the native sequence in the receptor.[7]

Thermodynamic studies between the HIPPENIFPLE peptide and the GCC : B10 monoclonal antibody using isothermal titration calorimetry showed that the interaction is exothermic and is associated with large changes in heat capacity.[8] Association was favoured at lower temperatures and involved hydrophobic forces. The dissociation constant was determined to be 1.72×10^{-6} M. The studies reported in this work constitute the generation of some important tools for GCC receptor studies, in addition to characterization of the structure and function of proteins involved in molecular signalling through GCC.

References

1 Hibbs, J. B. jr, Taintor, R. R and Vavrin, Z. — Macrophage cytotoxicity· role for L-arginine deiminase and imino-nitrogen oxidation to nitrite, *Science*, 1987, **235**, 473–476.

2. Kimura, H. and Murad, F. — Localization of particulate guanylate cyclase in plasma membranes and microsomes of rat liver, *J. Biol. Chem.*, 1975, **250**, 4810–4817.

3. Garbers, D. L. — Guanylate cyclase, a cell surface receptor, *J. Biol Chem*, 1989, **264**, 9103–9106.

4. Garbers, D. L. — Guanylyl cyclase receptors and their endocrine, paracrine and autocrine ligands, *Cell*, 1992, **71**, 1–4.

5. Nandi, A., Mathew, R. and Visweswariah, S. S. Expression of the extracellular domain of the human heat-stable enterotoxin receptor in *Escherichia coli* and generation of neutralizing antibodies. *Prot. Expression Purif.*, 1996, **8**, 151–159.

6. Nandi, A., Bhandari, R. and Visweswariah, S. S. Epitope conservation and immunohistochemical localisation of the guanylin/stable toxin peptide receptor, guanylyl cyclase C, *J. Cell Biochem.*, 1997, **66**, 500–511.

7. Nandi, A., Suguna, K., Surolia, A. and Visweswariah, S. S. Topological mimicry and epitope duplication in the guanylyl cyclase C receptor, *Prot. Sci.*, 1998, **7**, 2175–2183.

8. Swaminathan, C. P., Nandi, A. Visweswariah, S. S. and Surolia, A. Thermodynamics of the recognition of a cognate peptide epitope of guanylyl cyclase C by GCC : B10 monoclonal antibody (Poster and Abstract at the *10th Int. Congress in Immunology*, New Delhi, Nov. 1–6).

Thesis Abstract (Ph. D.)

Molecular mimicry by an antidiotypic monoclonal antibody to gonadotropin releasing hormone: Binding and signalling properties by K. Rajeswari
Research supervisors: Dr. Anjali A. Karande and Prof. A. Jagannadha Rao
Department: Biochemistry

1. Introduction

Gonadotropin-releasing hormone (GnRH) receptor is a member of the family of G-protein-coupled receptors (GPCRs) exhibiting the characteristic feature of the presence of seven transmembrane domains with three extracellular and three intracellular loops. Although pituitary is the major site of action of GnRH, binding sites for GnRH have also been located on various extra-pituitary tissues, viz. placenta, brain, breast, ovary, testis, lymphocytes and certain neoplastic tissues.[1] The molecular cloning of pituitary GnRH receptor cDNA encoding the receptor protein from several species, viz. human, rat, mouse, cow, sheep and cat-fish has led to investigations on the structural and functional aspects of GnRH receptor. Nevertheless, there is paucity of information on several aspects including the sites on the receptor involved in ligand binding and signal transduction and the mechanism of desensitisation of the receptor. Studies on GnRH-mediated signalling events reveal the possible involvement of dual pathways, viz. Ca^{++}-phosphokinase C (PKC) as well as cAMP-phosphokinase A (PKA) cascades[2], although the participation of cAMP-PKA pathway had been a subject of debate earlier. Antibodies have greatly facilitated the studies on biological receptors for several ligands, viz. insulin, luteinising hormone (LH), follicle-stimulating hormone (FSH), thyroid stimulating hormone (TSH), growth hormone and prolactin. It was therefore proposed to raise antibodies to GnRH receptor for use as tools in the studies on the receptor. Monoclonal antibodies (mAbs) were raised to the receptor using two different approaches, viz. antipeptide and anti-idiotypic approaches. This work deals with the characterisation of the two mAbs in terms of their receptor binding and signalling properties.

2. Materials and methods

mAbs F1G4 and A9E4 were obtained to a synthetic peptide corresponding to the extracellular domain (ECD) of human GnRH receptor.[3] These mAbs as well as an anti-idiotypic mAb, 4D10C1 raised earlier to the idiotype of a GnRH-specific mAb were tested for their ability to recognise the native GnRH receptor on various tissues and cell-lines in immunohistochemistry/cytochemistry and Western blotting.[4] The specificity was confirmed by ligand blotting using radiolabelled GnRH.

The signal-transducing properties of the mAbs were tested using cultures of human term placental villi[5] and rat pituitaries[6] wherein the levels of gonadotropins and cAMP were monitored in the presence of the mAbs. Using Ca^{++}-binding cell-permeable fluorescent dye and spectrofluorimetric analyser, the mAbs were also tested for their ability to mobilise intracellular Ca^{++} in a mouse gonadotroph cell line, viz. αT3-1.[4]

In order to study the role of cAMP-PKA pathway in GnRH/mAb-mediated signalling, the levels of GnRH/mAB-induced gonadotropins/cAMP were monitored in cultures of rat pituitaries in the presence of calcium channel blockers and a PKC inhibitor, viz. staurosporine. In all the signalling studies, an antagonist of GnRH was employed to establish specificity of the binding of the mAb to the GnRH receptor.

3. Results and discussion

While the anti-idiotypic mAb, viz. 4D10C1 was found to recognise GnRH receptors from several mammalian tissues as demonstrated by immunohistochemistry and Western blotting[4], the antipeptide mAb, viz. F1G4 showed binding to GnRH receptors of human origin only.[3] Although mAb A9E4 showed binding to the ECD peptide, it failed to recognise native GnRH receptor protein. Next, the signal-transducing abilities of the antipeptide and anti-idiotypic mAbs were tested using *in vitro* cultures of human-term placental villi and rat pituitaries. A dose-dependent increase in the levels of hCG secretion was seen in placental cultures upon stimulation by mAb 4D10C1. Likewise, the mAb also induced the levels of LH and FSH in rat pituitary cultures. The antipeptide mAb, viz. F1G4 neither stimulated nor inhibited GnRH-mediated gonadotropin release. Mab 4D10C1 was also shown to induce calcium influx in a mouse gonadotroph cell line, viz. αT3-1.[4] That the activation by the antibody is due to binding to GnRH receptors was confirmed by prior incubation with a well-characterized GnRH receptors was confirmed by prior incubation with a well-characterized GnRH antagonist which blocked the activation by the mAb. In all instances of the mAb-mediated response, the concentration of the antibody required to bring about saturating levels of induction was about five fold lower than that of GnRH. This could be due to the labile nature of GnRH in comparison to the mAb owing to the presence of protease-sensitive sites on the decapeptide. The other possible reasons could be the higher affinity of the mAb for the receptor compared to GnRH as well as the ability of antibodies to bring about receptor crosslinking.

Apart from the well-studied PKC pathway involving Ca^{++} and diacylglycerol (DAG) as second messengers in the GnRH-mediated receptor signalling, there are several lines of evidence to show the involvement of cAMP-PKA in the signalling cascade.[2] The effect of mAb 4D10C1 on the levels of cAMP was therefore investigated in cultures of human-term placental villi as well as rat pituitaries. A dose-dependent increase in the levels of cAMP was seen upon stimulation by the mAb as with GnRH. Moreover, forskolin, a nonspecific stimulator of cAMP, was shown to induce the secretion of LH and FSH in a dose-dependent manner, suggesting a role for cAMP in the mAb/GnRH-induced activation process. When similar experiments were carried out in the presence of calcium channel blockers or staurosporine, decreased levels of gonadotropins as well as cAMP were observed suggesting the possibility of cross-talk between the Ca^{++}-PKC and cAMP-PKA pathways in GnRH-mediated signalling. From all the observations made in this study, it becomes evident that the anti-idiotypic mAb mimics GnRH in terms of its signalling properties. This prompts its application in the better understanding of the role of the GnRH receptor.

References

1. Sealfon, S C., Weinstein, H and Millar, R. P	*Endorince Rev.*, 1997, **18**, 180–205.
2. Delhaye, R *et al.*	*Molec. Cell Endocrionol*, 1997, **135**, 119--127.
3 Karande, A. A. *et al*	*Molec. Cell Endocrinol.*, 1995, **114**, 51–56.
4. Karande, A. A. *et al*	*Biochem. Molec. Biol. Int.* (in press).
5 Siler-Khodr, T. M. *et al.*	*Biol. Reprod.*, 1986, **34**, 245–254.
6. Sen, K. K and Menon, K. M. J.	*Biochem. Biophys. Res. Commun* , 1979, **87**, 221–228.

Thesis Abstract (M. Sc. (Engng))

Design and synthesis of novel dimeric lipids and amphiphiles and characterisation of their vesicular and micellar properties by Soma De

Research supervisor: Dr Santanu Bhattacharya
Department: Organic Chemistry

1. Introduction

While the properties of vesicular membranes derived from a large number of *monomeric* natural lipids such as phosphatidylcholines as well as their synthetic analogues have been examined in detail, there is very little in the literature that attempts to examine the vesicles-prepared *multimeric* lipids. For quite sometime, we have been interested in establishing the relation between amphiphile molecular architecture and properties observed upon their self-organization. Here we describe the biophysical and morphological aspects of various supramolecular organizations generated from newly developed *dimeric* lipids and amphiphiles that are covalently connected by a spacer chain at the level of head group.

2. Ion-paired amphiphile systems

2.1. *Flexible polymethylene spacer near head group*

A series of vesicle-forming ion-paired *bis*(hexadecyl dimethylammonium)alkane dipalmitate amphiphiles where the two headgroup charges are separated by a flexible polymethylene chain $[-(CH_2)_m-]$ such that the conformation of the spacer chain determines the intra monomer head group separation has been synthesized. Employing a wide range of physical techniques such as electron microscopy (characterization of aggregate shapes), fluorescence spectroscopy (membrane permeability via dye entrapment, rigidity of bilayers, phase transition), differential scanning calorimeter (phase transition), X-ray diffraction (orientation of ion-pairs in mem-

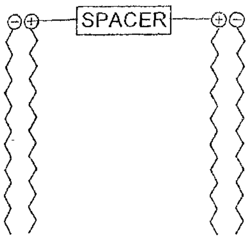

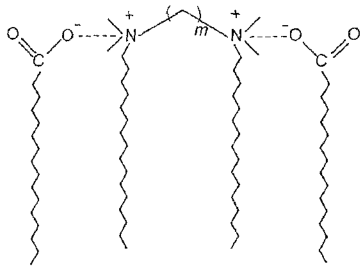

1a - 1h, m = 2, 3, 4, 5, 6, 8, 10, 12

branes) and molecular modeling, the aggregates have been characterized. The results indicate that the gemini biscationic surfactants from vesicular aggregates with corresponding ion pairs with palmitic acid and the aggregate characteristics such as thermal stability, permeability, etc. can be rationally modulated by varying spacer chains.[1, 2]

Another class of ion-paired amphiphiles, i.e. *bis*(hexadecyl dimethylammonium)alkane-*bis*(hexadecyl phosphate) amphiphiles, **2a–2d** in which the -Nme$_3^+$...-OOC$^-$ head groups have been replaced by the -Nme$_3^+$... $^-$O-P(O)OR-O(CH$_2$)$_m$OP(O)OR-O$^-$...$^+$Me$_3$N– head groups (phosphatidyl-choline mimic) has also been synthesized with the aim to study the dynamics of the head group indirectly governed by the nature of the spacer by ^{31}P NMR spectroscopy. In addition to the techniques mentioned above, ^{31}P NMR spectroscopy and paramagnetic relaxation methods are also used to derive information about various membrane phases formed by them and the transbilayer lipid distribution. These systems do exhibit distinct differences in morphological and biophysical properties as a function of spacer.

2.2. *Hybrid bolaphile/amphiphile ion-paired system*

Three new hybrid (bolaphile-amphiphile) ion pairs, *bis*(hexadecyl trimethylammonium)-phenyl-1, 2-, 1, 3- and 1, 4-di(oxyundecanoate), **3**, **4** and **5** where the bolaamphiphilic counterions originate from the different isomeric positions of the central phenyl ring, and the corre-

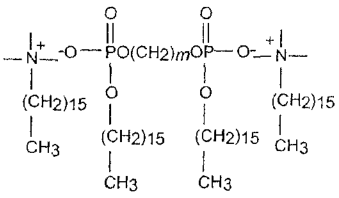

2a - 2d, m = 2, 4, 6, 10

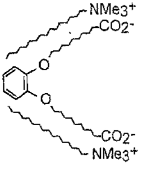

3

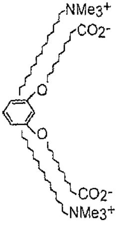

4

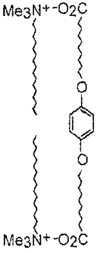

5

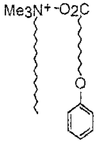

6

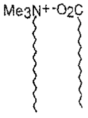

7

sponding (monopolar) anion/cation pairs cetyltrimethylammonium (CTA) 11-phenoxy undecanoate, **6** and **CTA** palmitate, **7** were synthesized and their vesicular properties have been studied using various physical methods. Not only the membrane organization in these vesicles is widely different, but also they exhibit interesting phase transition and permeability behavior. Thus, it was shown that by judicious incorporation of central, isomeric, disubstituted aromatic units as structural anchors into different bolaphiles, one can modulate the properties of the resulting vesicles.[3]

3. Dimeric pseudoglyceryl biscationic lipids

A study on synthesis and vesicle formation from another series of eight new *gemini biscationic* pseudoglyceryl lipids, **8a–8h** where the two dimethylammonium ion head groups are separated by variable number of polymethylene units [-$CH_2)_m$-] was carried out. The vesicle sizes and morphologies were found to depend strongly on m-value, the method, and the thermal history of the vesicle preparation. Strikingly, the T_m values for the vesicular **8a–8h** revealed a nonlinear dependence of T_m values on m-value. These vesicles were able to entrap small water-soluble solute and sustain transmembrane pH gradients. Reflection X-ray diffraction of the cast films elucidated the nature and the thickness of these membrane organizations and it was revealed that they form three different kinds of membrane architectures depending on the m-value. The ESR spin probe method using doxylstearic acids, spin-labeled at various positions were used to establish the chain flexibility gradient and homogeneity of these bilayer assemblies. The fusion characteristics of these bipolar tetraether lipids were examined in the presence of sodium sulfate using fluorescence resonance energy-transfer fusion assay. With the aid of molecular modeling studies, structural reasons for these unusual findings at membrane level

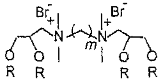

R $= n\text{-}C_{16}H_{33}$ $m = 3, 4, 5, 6, 12, 16, 20, 22$

8a - 8h

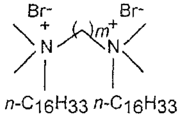

9a - 9g, m = 3, 4, 5, 6, 8, 10, 12

have been assigned. The interactions of cholesterol with this set of lipids are highly dependent on the m-value. Thus we have demonstrated yet another example of gemini lipid system in which the membrane properties can be fine-tuned by simple structural changes at the lipid monomer level.[4]

4. Physical and morphological behavior of dimeric micellar aggregates

Another important group of organized assemblies is micellar aggregates. We have studied the role of spacer chain in dimeric micellar organization using the techniques of small-angle neutron scattering and fluorescence spectroscopy.[5]

We have synthesized different dimeric amphiphiles Br^-, n-$C_{16}H_{33}NMe_2{}^+$-$CH_2)_m$ N^+Me_2-n-$C_{16}H_{33}$, Br^- (where $m = 3$, 4, 5, 6, 8, 10 and 12), **9a–9g**, which adopt different morphologies and internal packing arrangements in aqueous media depending on their spacer chain length (m). Detailed measurements of small-angle neutron scattering (SANS) cross-sections of these *bis*-cationic, dimeric surfactant micelles in aqueous media (D_2O) have been reported. The data have been analyzed using the Hayter and Penfold model for macro-ion solution to compute the inter-particle structure factor S(Q), taking into account the screened coulomb interactions between the dimeric micelles. The SANS analysis clearly indicated that the extent of aggregate growth and the variation of shapes of the dimeric micelles depend primarily on the spacer chain length. With spacer chain length, $m \leq 4$, the propensity of micellar growth is particularly pronounced. The critical micelle concentrations (CMC) and their microenvironmental features, namely, the microviscosities that the dimeric micellar aggregates offer to a solubilized, extrinsic fluorescence probe, 1, 6-diphenyl-1, 3, 5-hexatriene are also determined. The changes of CMCs and microviscosities as a function of spacer chain length have been explained in terms of conformational variations and progressive looping of the spacer in micellar core upon increasing m values. Similar studies for different mixed micelles composed of CTAB and **9a**, **9c** and **9f** in aqueous media (D_2O) are also investigated. It indicated that the extent of aggregate growth and the variation of shapes of the mixed micelles could be modulated by the amount of dimeric surfactant present in these mixtures.

Similar study was also extended to a closely related amphiphilic system containing mono-, di- and tri-oxyethylene spacer chains. The SANS analysis showed that the micellar morphology depends both on the nature and the length of the spacer unit.

References

1. Bhattacharya, S. and De, S. *J. Chem. Soc. Chem. Commun.*, 1995, 651–652.
2 Bhattacharya, S. and De, S. *Langmuir*, 1999, **15**, 3400–3410.

3 Bhattacharya, S., De, S. and Subramaniam, M. — *J Org Chem*, 1998, **63**, 7640.
4. Bhattacharya, S. and De, S. — *Chem Eur. J*, 1999, 5, 2335–2347
5a. De, S. *et al.* — *J. Phys. Chem.*, 1996, **100**, 11664.
5b. De, S. *et al.* — *J. Phys Chem B*, 1998, **102**, 6152

Thesis Abstract (Ph. D.)

Bénard–Marangoni convection and instability in a layered fluid system by Purna Chandra Biswal
Research supervisor: Prof. A. Ramachandra Rao
Department: Mathematics

1. Introduction

Buoyancy-driven instability has been well established since the pioneering work of Rayleigh[1] who showed that convection, called Bénard convection[2], occurs only when the Rayleigh number which is a ratio of buoyancy force to the dissipative force exceeds a critical value. On the other hand, Pearson[3] showed that surface-tension-gradient effects can also cause convection, usually called Marangoni convection[4] when the Marangoni number which is a ratio of thermocapillary force to the dissipative force exceeds a critical value. Inhomogeneities in solidified electronic materials have a very undesirable effect on the material's electronic properties. Therefore, in the processing of high-quality electronic materials, stringent control of electronic melt stoichemistry is required during the solidification process. One source for inhomogeneities in the solidified crystal is thermal convective flow in the liquid melt. Thus, the control of melt convection affords control of crystalline structure. Therefore, it is necessary to develop methods and mathematical models to suppress thermal convection caused by buoyancy and surface tension forces. A reduction in the convection due to buoyancy is achieved in a microgravity environment. The rotation of a liquid column to confine thermocapillary or Marangoni convection near the surface is another technique to suppress convection. Favorable results of reduced convection are also reported using an applied magnetic field. Another alternative method has been proposed, whereby the liquid metal layer is encapsulated by another immiscible and noncorrosive liquid layer to suppress any thermocapillary convection that may develop in space processing. This method has several other advantages, namely (i) one can enhance or reduce the convection as needed by selecting a liquid encapsulant with appropriate physicochemical properties, and (ii) a fluid-fluid system will not develop thermal stress problems at the phase boundary as in solid encapsulation. Motivated by this, several workers have studied the thermocapillary convection in two-immiscible liquid layers with flat free surface and flat liquid–liquid interface with differential heating applied parallel or normal to the interface.

This work is devoted to the study the Bénard–Marangoni convection and instability in two-layered immiscible viscous liquid systems or a single-layer system with or without magnetic field in finite or infinite domains.

2. Thermocapillary convection in two immiscible liquid layers with curved free surface

Steady thermocapillary convection is investigated in a system of two superposed layers of immiscible, incompressible, viscous liquids with a curved free surface and a flat liquid–liquid interface in a configuration similar to that of an encapsulated crystal growth. The layers are bounded on the sides by isothermal vertical walls maintained at different constant temperatures. An analytical solution is obtained for infinite layers under lubrication approximation aspect ratio A (ratio of length of the cavity to height of the cavity) $\rightarrow 0$. There exist four different flow regimes under zero gravity condition depending on the values of λ, the ratio of the temperature coefficient of the interfacial tension to that of the surface tension. The solutions for the core flow, temperature and the free surface are determined for a finite domain by using matched expansion with the aspect ratio A (small) as a parameter correct to $O(A^2)$. In obtaining the solutions, we have used either fixed lines or fixed angles at the contact between the free surface and the side walls. Streamlines for the flow near the vertical boundary are determined numerically using finite-difference over relaxation method with suitable relaxation parameter and matching it with the analytical solution for the stream functions in the core region. In general, the free surface is not flat and the conditions under which it becomes flat are presented. It is observed that the strength of the vortices near the walls, the free surface height and bending of the isotherms are closely connected and depend on the value of λ. Further, for certain value of $\lambda = 0.5$, it is observed that there is no flow in lower layer called halt condition as it halts the fluid motion. The results for a single layer can be obtained by taking (i) the viscosity of the lower layer very large tending to infinity or (ii) the width of the lower layer tending to zero or (iii) by taking the fluid properties to be the same for both the fluids. We have obtained the analytical results for a single layer by taking the viscosity of the lower layer tending to infinity

3. Thermocapillary convection in two-layer liquid systems with deformed interfaces

Analysis of the steady thermocapillary convection of two superposed layers of immiscible incompressible, viscous liquids with deformed free surface and flat liquid–liquid interface in a configuration similar to that of an encapsulated crystal growth has been extended to the case with both interface and free surface being deformed. The analytical solutions are presented for the stream function and temperature are presented correct to $O(A^2)$. The shapes of free surface and interface are determined for different parameters and the effect of these parameters on streamline structure is also analyzed using fixed contact lines or fixed contact angles. In the absence of appropriate numerical techniques to deal with the problem in which the shapes of interface and free surface are not known a priori the solutions for streamlines, temperature, interface and free surface shapes presented here give some insight into the flow structure. The structure of the streamlines and the isotherms for deformable interface and free surface qualitatively remains the same as that for flat interface and free surface. It is observed that for a given fixed angles of contact the shape determined for the free surface is convex and the corresponding shape for the interface is either convex or concave depending on the value of λ. The critical parameters which make the interface and free surface flat are determined. The assumption of flat interface and free surface is good for certain fluids with appropriate parameters.

4. Thermal convection in two immiscible liquid layers with a uniform magnetic field

The effect of uniform magnetic field on thermal convection in a shallow cavity, with differentially heated side walls, filled with two viscous, immiscible, incompressible and electrically conducting fluids in the presence of buoyancy force is studied. The fluid–fluid interface and the free surface are assumed to be flat and the driving forces for the flow are the thermocapillary and buoyancy forces. Closed-form solutions, under thin-layer approximation, neglecting the side wall effects, are obtained for the stream function and temperature. In various limiting cases, namely, (i) absence of buoyancy force, (ii) absence of thermocapillary force and (iii) absence of magnetic fields, the solutions are obtained and they coincide with the existing results in the literature. The velocity is calculated and the resulting cell patterns are discussed for different values of λ and H_a (Hartmann number). Here also there exist four different flow regimes depending on the values of λ but with reduced convection compared to the non-magnetic case. It is observed that the halt condition decreases with an increase in H_a and for $\lambda < 0.5$ it is possible to control the convection in the lower layer by a suitable choice of the magnetic field.

5. Steady thermal instability in a two-layer system of conducting fluid

The onset of steady Bénard–Marangoni convection in two horizontal liquid layers of electrically conducting immiscible, viscous, incompressible fluids subjected to a uniform vertical magnetic field and temperature gradient is analyzed using a combination of analytical and numerical techniques. The free surface is either deformable or nondeformable and the interface is always flat. The effect of the lower layer on the critical values of Rayleigh, Marangoni and wave numbers for the onset of pure Marangoni convection are increased whereas the critical parameters for the onset of pure Bénard convection are decreased compared with the single-layer model. Critical Marangoni and wave numbers are found to increase with an increase in λ, the ratio of temperature coefficient of surface tension at the interface to that at the free surface, for pure Marangoni convection in the presence of magnetic field. All disturbances can be stabilized with sufficiently strong magnetic field when the free surface is non-deformable and insulated. If the free surface is allowed to deform and gravity waves are excluded then the layers are always unstable to disturbances with sufficiently small wave number with magnetic field. Inclusion of gravity waves has a stabilizing effect on certain disturbances of small wave number in the presence of weak or moderate magnetic field. The results for a single layer and for two layers are qualitatively similar when the free surface is deformable. It is observed that if the ratio of lower layer to the upper layer is greater than one then the critical value for stability of Marangoni convection increases whereas it decreases for Bénard convection. All results obtained in the present work agree with those obtained earlier in literature for a single layer in the limit of the height of the lower layer tending to zero.

6. Oscillatory Marangoni instability in a two-layer system of conducting fluid

The effect of magnetic field and encapsulated layer on the onset of oscillatory Marangoni instability in two infinite horizontal immiscible, incompressible, viscous, electrically conducting liquid layers is investigated using normal mode analysis. The characteristic equation with complex coefficients is solved numerically by varying the frequency parameters until one gets a a real Marangoni number as a solution. Oscillatory Marangoni instability is possible when the free surface is deformable and the interface is flat for certain negative Marangoni numbers (heated from top). When the free surface is flat and the interface is deformed there is no overstability in the absence of magnetic field. If both free surface and interface are deformed onset of overstability depends on the parameter Λ, the ratio of surface tensions at free surface and interface. Further, it is observed that if the lower layer height is more than that of the upper layer then the oscillatory convection is more stable. The corresponding single layer results with or without magnetic field are obtained by taking the fluid properties to be the same for both the fluids considered.

7. Thermal instability in a three-dimensional rigid container with prescribed heat flux at lower boundary

The Bénard–Marangoni convection in a three-dimensional container with rigid lateral walls and prescribed heat flux at lower boundary is studied. The upper surface of the single layer of incompressible viscous fluid is assumed to be flat with temperature-dependent surface tension. A Galerkin–Tau method with odd-and-even trial functions satisfying all the natural boundary conditions except the essential boundary conditions at the free surface has been used to solve the problem. The critical Marangoni and Rayleigh numbers are determined for the onset of steady convection at the threshold as a function of aspect ratios a_1 (ratio of length to height) and a_2 (ratio of breadth to height) for the cases of Bénard–Marangoni, pure Marangoni and pure Bénard convections. Flow structures at the threshold are calculated for all the cases. The influence of Biot number on the critical parameter is also analyzed. The critical parameters for the heat flux prescribed case are higher than those for the case with prescribed temperature at the lower boundary.

Reference

1. LORD RAYLEIGH	On the convection currents in a horizontal layer of fluid when the higher temperature is on the under side, *Phil. Mag.*, 1916, **32**, 529–546.
2. BENARD, H.	Les Tourbillons cellularies dans une nappe liquide, *Revus générale Sci. pures appliquées*, 1900, **11**, 1261–1271, 1309–1328.
3. PEARSON, J. R. A	On convection cells induced by surface tension, *J. Fluid Mech.*, 1958, 4, 489–500.
4. MARANGONI, C.	Ueber die Ausbreitung der Tropfen einer Flussigkeit aut der oberflache einer anderen, *Ann. Phys. Chem.*, 1871, **143**, 337

Thesis Abstract (Ph.D.)

Studies on the effect of thermal annealing, hydrogen and nitrogen plasma treatments in bulk cadmium telluride by Suma Gurumurthy
Research supervisors: Profs. Vikram Kumar and H. L. Bhat
Department: Physics

1. Introduction

In the past three decades, CdTe and related alloys have been a subject of intense study due to their potential application in infrared and X-ray detectors and their use as a substrate for growth of $Hg_{1-x}Cd_xTe$.[1] The use of CdTe in active device applications and as a substrate for IR detectors requires the availability of good quality, large single crystals. This is quite demanding because of the problems encountered during their growth and the presence of large concentration of defects. The study of these defect levels is extremely complex. The origin of many deep levels still remains unclear. A lot of work is being carried out with respect to the understanding of the creation of native defects, their interactions with dopants and residual impurities, etc. In the present work, an attempt has been made to study various types of defects, particularly the deep levels by thermal annealing, elimination of these levels by hydrogenation and the effect of rf nitrogen plasma exposure on the CdTe samples.

2. Experimental

The present investigation was carried out on undoped and indium-doped single crystals of CdTe, grown at Solid State Physics Laboratory, Delhi, by the asymmetrical and horizontal Bridgman techniques.[2] Cadmium and tellurium annealings were carried out by placing the samples in a sealed evacuated dumb bell-shaped ampoule in the presence of excess cadmium or tellurium vapor pressure. Vacuum annealing was done by placing the sample in an evacuated ampoule without cadmium or tellurium. Annealings were carried out at 650°C for 6 and 12 h.

Hydrogen plasma exposure was carried out by placing the samples in a downstream plasma in a parallel plate reactor operating at a frequency of 13.56 MHz. Hydrogenations were carried out at a temperature of 150°C for 1 h in a pressure of 0.5 torr and a plasma power density of $0.5 W/cm^2$. Reverse-bias annealing (RBA) experiments were performed on hydrogenated samples at different temperatures at 3 V for different times ranging from 10–45 min.

Nitrogen plasma exposure (NPE) was also carried out in the down stream geometry on both the doped and undoped CdTe. The nitridation conditions were however, found to be quite different from the hydrogenation conditions.[3] The NPE was carried out at a substrate temperature of 300°C for 5 hours at a pressure of 0.5 torr and a plasma power density of $1 W/cm^2$.

PL measurements were carried on all the sets of processed samples at 4.2 K using the FTPL system. Excitation intensity dependence as well as temperature dependence of the PL were carried out on most of the samples. Back ohmic contacts to the n-CdTe samples were made by depositing indium and annealing at 160°C for 2 min in hydrogen atmosphere. Gold Schottky dots of 0.6 mm diameter were deposited through a metal shadow mask. Conventional I–V and C–V measurements were carried out on the hydrogenated and nitrided, (doped) CdTe samples. SEM, XPS and SIMS were some of the other techniques that were used to characterise the CdTe samples.

3. Results and discussion

Detailed PL studies carried out on samples annealed under vacuum, Cd over pressure and Te over pressure showed the 1.11eV peak to involve transitions via a native defect level related to a cadmium vacancy. Two previously unreported peaks are observed in undoped CdTe at 1.135 eV and 1.21 eV. The 1.135 eV peak which shows up after long hours of cadmium annealing is thought to be related to some cadmium interstitial complex. In indium-doped samples, a new peak at 1.146 eV is seen to appear after cadmium annealing. On systematic annealing studies the origin of this peak as arising due to transitions from the conduction band to an acceptor involving a tellurium vacancy is established.[4] 1.21 eV peak is related to some growth defect (strain). This peak was absent in the indium-doped samples indicating the reduction of strain due to doping. Optical microscopy was carried out to study the surface morphology of the samples after annealing. The vacuum annealed sample surface showed triangular thermal etch pits whereas the cadmium-annealed sample did not show any etch pits and more or less resembled the control sample surface.

The effect of hydrogen plasma exposure on the electrical and optical properties of low and high resistivity indium-doped and undoped CdTe has been investigated. Plasma treatments were carried out at different temperatures ranging from 90–250°C. Surface damage by ion bombardment was found to compete with passivation. The surface damage during the plasma exposure was overcome for certain optimized plasma power density and distance between the plasma plates and substrates holder. C–V measurements showed that hydrogen incorporated in n-CdTe at 150°C, strongly reduces the indium donor activity (Fig. 1). The thermal stability of the dopant passivation was studied by carrying out reverse-bias annealing (RBA) experiments at various temperatures. The observed evolution of the dopant profiles after RBA measurements suggested the presence of H^- charge state of hydrogen in n-CdTe. Donor passivation in n-CdTe has been explained by the formation of neutral donor–hydrogen complexes. The reactivation of donors under RBA however seemed to be different from that of other well-studied semiconductors, the main difference being the low reactivation of the donors near the surface.

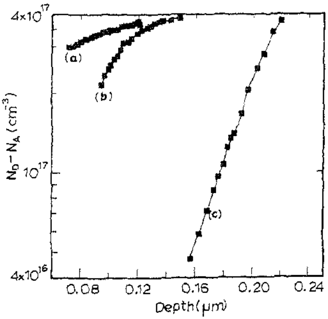

FIG. 1. Net active donor concentration profiles for (a) control, (b) hydrogenated at 170°C and (c) hydrogenated at 150°C.

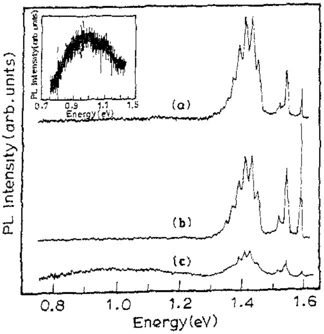

FIG. 2. PL spectra at 4.2 K of low resistivity CdTe:In. (a) control, (b) hydrogenated at 210°C, (c) hydrogenated at 250°C. (The inset shows the peak at 1 eV for the sample hydrogenated at 250°C

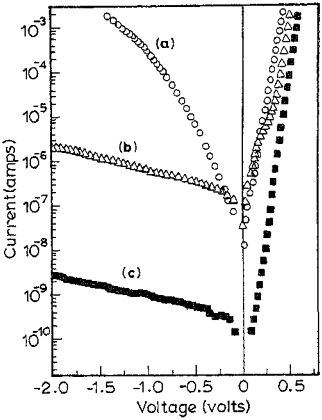

FIG. 3. I–V characteristics (semi-log plot) of (a) control, (b) argon plasma exposed, (c) NPE Au/n-CdTe diodes at room temperature (argon plasma and NPE duration: 5 hours).

The donor passivation in low resistivity indium-doped CdTe as studied by PL spectroscopy also showed efficient passivation to occur around 150°C. Passivation of deep non-radiative centers like surface states, grain boundaries, dislocations, etc. is seen up to 210°C as an increase in the luminescence intensity (Fig. 2). However, for hydrogenation carried out at temperatures around 250°C and PL yield was found to reduce drastically along with the evolution of the deep luminescence band at 1.1 eV indicating surface damage (Fig. 2). Passivation of acceptors in undoped CdTe was indicated by the decrease of the acceptor-bound excitonic luminescence at 1.589 eV upon hydrogenation. This has been explained by the formation of neutral acceptor hydrogen complexes.

Nitrogen plasma exposure (NPE) effects were studied in moderately and heavily doped CdTe with indium. The I–V characteristics of Au/n-CdTe Schottky diodes were found to improve dramatically after NPE. This is shown in Fig. 3. Also shown in this figure are the characteristics for the control and the argon plasma-exposed samples. The reverse saturation currents were found to drop by nearly four orders of magnitude after NPE. The forward I–V plot in the NPE samples was found to be nearly ideal over several decades of current indicating the dominant current transport to be purely thermionic in nature. The effective barrier height obtained from the temperature dependence of the I–V characteristics was found to increase from approximately 0.79 eV in the control to 1.03 eV in the NPE sample. Measurements on different metal Schottky diodes indicated Fermi-level pinning suggesting creation of acceptor-like surface states. SEM micrographs showed no surface damage on the nitrided samples.[5] The breakdown characteristics were also found to improve drastically after NPE, with a breakdown voltage as high as 20 volts. Temperature-dependence studies showed a change in the breakdown mechanism from Zener to Avalanche in the NPE diodes, suggesting a change in the doping concentration close to the surface.

C–V depth profile of the NPE samples showed the indium donor concentration to reduce at the surface. This drop has been attributed to a complexation and compensation process occurring due to the introduction of certain number of acceptors through the plasma. Absence of nitrogen in the bulk was confirmed from SIMS and XPS measurements thereby ruling out a passivation process. With the help of PL measurements these acceptors have been assigned to cadmium vacancies and their complexes with the indium donors. A plausible model has been put forward to explain the compensation process in the bulk. The thermal stability of the plasma-exposed samples up to 350°C enables high-temperature processing of the samples for device fabrication. Nitrogen plasma exposure carried out on Schottky barrier solar cells would, hence, result in higher open-circuit photovoltages and higher photoconversion efficiencies. No aging problem was seen in the NPE diodes.

References

1. KHAN, A. A. *et al.* *J. Electron. Mater.*, 1986, **15**, 181–187.
2. BAGAI, R. K. AND BORLE, W. N. *J. Cryst Growth*, 1989, **94**, 561–564.
3. SUMA GURUMURTHY, *et al.* *Appl. Phys. Lett*, 1996, **68**, 2424–2426.
4. SUMA GURUMURTHY, *et al.* *Bull. Mater. Sci*, 1994, **17**, 1057–1064
5. SUMA GURUMURTHY, BHAT, H. L. AND VIKRAM KUMAR *Int. Autumn Meeting on Gettering and Defect Engineering in Semiconductor Technology*, Spa, Belgium, October 1997.

Thesis Abstract (Ph.D.)

Phase selection and phase evolution in the MgO-MgAl$_2$O$_4$ system under non equilibrium processing conditions

by Tania Bhatia
Research supervisors: Profs Vikram Jayaram and Kamanio Chattopadhyay
Department: Metallurgy

1. Introduction

The response of the MgO-MgAl$_2$O$_4$ system to two different non-equilibrium processing conditions has been studied. The choice of the system was based on the availability of reliable thermodynamic data[1] that was extrapolated and used to explain the phase selection and phase evolution in the system. The equilibrium phases in the system, periclase (MgO) and spinel (MgAl$_2$O$_4$), are line compounds at temperatures as high as 1300 K. Chemical precursor pyrolysis was used to achieve large departures from equilibrium in the system and rapid solidification served as a point of comparison since the two techniques accessed different temperature domains of the phase diagram. During precursor pyrolysis, inorganic (or metallorganic) salt solutions decompose at low temperatures to result in oxides, which is akin to crystallisation at very low homologous temperatures and the menu of metastable phases available to the system is enhanced.[2]

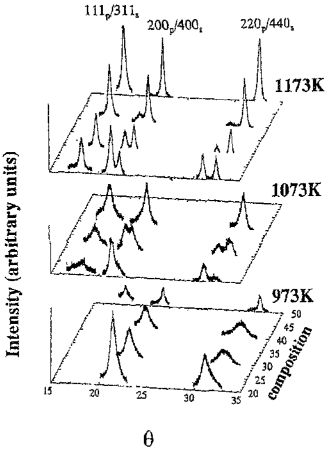

FIG. 1. Composite diffraction pattern which depict the effect of heat treatment on spray-pyrolysed MgO-$MgAl_2O_4$. These show the phases present as a function of composition and temperature of heat treatment.

2. Experimental

Aqueous solutions of aluminium and magnesium nitrates were mixed in the ratio required to yield MgO-20, 30, 40 and 50 mol% Al_2O_3. Two methods of achieving thermal decomposition were (i) drying at 473 K and (ii) spray pyrolysis at 673 in a borosilicate/Pt dish. Heat treatments were carried out in a Pt crucible.

Ceramic rods (of composition MgO-20, 30 mol% Al_2O_3) were prepared using MgO and Al_2O_3 powders and melted using an oxyacetylene flame. The molten droplets were rapidly solidified in a twin roller quenching set up with steel rolls. The linear velocity at the point of contact between the rolls was 30 m/s.

Resulting phases were identified using X-ray diffraction (Huber Guinier diffractometer model 642; CuK_α) and transmission electron microscopy (Jeol, 2000 FX II).

3. Results and discussion

Segregation free, homogeneous (Mg, Al)O solutions were produced by pyrolysis of the nitrate solutions at 673 K and the phase evolution of the oxides studied. Figure 1 is a composite XRD pattern which shows the effect of heat-treatment temperature on the phase evolution in the spray-pyrolysed powders. Table I summarizes the phase present as a function of temperature

Table I
Phases identified in MgO-$MgAl_2O_4$ processed by spray pyrolysis of nitrate precursors at 673 K and subsequent heat treatment

Temperature of heat treatment →	As sprayed	973 K/1h	1073 K/1h	1173 K/1h
MgO-20 mol% Al_2O_3	Periclase	Periclase	Periclase + Spinel	Periclase + Spinel
MgO-30 mol% Al_2O_3	Periclase	Periclase	Periclase + Spinel	Periclase + Spinel
MgO-40 mol% Al_2O_3	Periclase*	Periclase	Spinel	Periclase + Spinel
MgO-50 mol% Al_2O_3	Amorphous	Spinel	Spinel	Spinel

*difficult to establish as the peak is very broad.

and composition. It is seen that in the competition between spinel and periclase, the first nucleating phase in all compositions up to 40 mol% Al_2O_3 is periclase. This is the first report of such a high quantity of Al_2O_3 dissolved in periclase. Only in the stoichiometric composition (50% Al_2O_3) did spinel nucleate and grow. In the 20 and 30 mol% Al_2O_3 compositions, the supersaturated periclase transformed to the two equilibrium phases by solute partitioning. In the 40 mol% Al_2O_3 composition, periclase transforms in a partitionless manner to spinel at 1073 K which renucleates periclase at 1173 K. From Fig. 2a it can be seen that except for the 20% Al_2O_3 composition, the driving force for partitionless transformation from liquid to spinel is higher. The preference for the crystallisation of periclase at 973 in compositions up to 40 mol% Al_2O_3 is shown to be because of the higher nucleation rate for its crystallisation (Fig. 2b).

It is found that drying the nitrate solutions at 473 K results in the formation of compositionally inhomogeneous, segregated oxide mixtures. It has been suggested that segregation is caused by the difference in solubility of the individual nitrate salts in water. The distinguishing feature of the segregated powders is the appearance of stoichiometric periclase with grain size

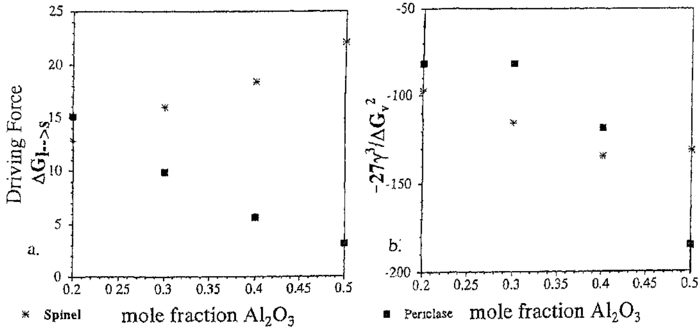

FIG. 2a. Relative driving force for partitionless crystallization of periclase and spinel (b) Nucleation rate of the periclase and spinel as a function of composition estimated at 1000 K.

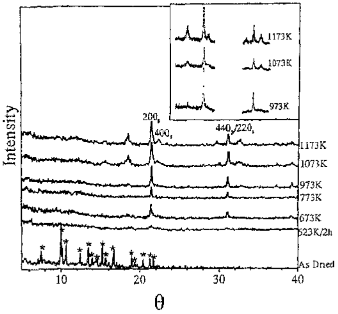

FIG. 3. Effect of heat treatment on MgO-20 mol% Al_2O_3 prepared by drying nitrate precursors at 473 K. Starting powders were not homogeneous.

in excess of 0.3 μm at temperatures are as low as 973 K (Fig. 3). The key to obtaining fine-grained periclase is to be able to synthesise (MgAl)O solid solutions with the rock salt structure. The resistance of periclase solid solutions to coarsening as seen in the pyrolysed powders is possibly due to the formation of a large concentration of point defects that could have a tendency to order.

The transformations in the 30 mol% Al_2O_3 composition allows the comparison of the thermodynamic and kinetic criteria operating under different processing conditions. In the competition between periclase and spinel it has been shown that a higher temperatures and low un-

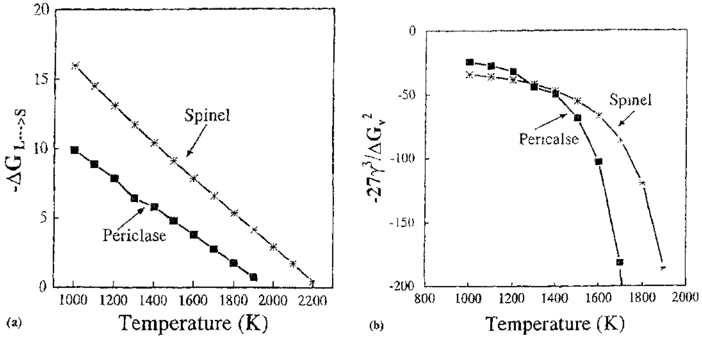

FIG. 4. The driving force for the 30 mol% liquid to transform to periclase and spinel as a function of temperature. (b) Nucleation rate for spinel and periclase as a function of temperature.

dercoolings as in the case of RSP, partitionless transformation of liquid to spinel is favoured by virture of a higher driving force and a higher nucleation rate (Fig. 4). At lower temperatures, accessed through spray pyrolysis, although spinel has a higher driving force, nucleation favours the formation of periclase.

4. Summary

1. This works as a qualitative and quantitative comparison precursor pyrolysis and rapid solidification with aid of the MgO-$MgAl_2O_4$ pseudo-binary system. The criteria for phase selection and evolution by thermal decomposition and RSP has been explained on the basis of thermodynamic and kinetic arguments.
2. Pyrolysis expands the range of metastable materials producible. It has been possible to extend in solid solubility of Al_2O_3 in MgO substantially. (Previous reports were up to 20% Al_2O_3 and in this study (MgAl)O solution of composition 40 mol% Al_2O_3 was synthesised).
3. The importance of obtaining homogeneous segregation-free solid solutions has been recognised. To avoid segregation, the (multi-component) nitrate solutions need to be heated rapidly up to temperatures above which the solution decomposes as a single solution.
4. New structure intermediates between spinel and periclase have been postulated to explain a stable composition modulation in spinel (formed by RSP).

References

1. BENGT HALLSTEDT	Thermodynamic assessment of the system MgO-Al_2O_3, *J Am. Ceram. Soc.*, 1992, **75**, 1497.
2. LEVI, C. G.	Metastability and microstructure evolution in the synthesis of inorganics from precursors, *Acta Mater.*, 1988, **46**, 747.

Thesis Abstract (Ph.D.)

Semi-active vibration isolation using constant force devices by Y. Krishna
Research supervisors: Prof. U. Shrinivasa and Dr. B. S. Sarma (Orgn)
Department: Mechanical Engineering

1. Introduction

The control of mechanical vibration and shock is a prime consideration in designing to withstand the damaging effects of modern dynamic environments. Vibration or shock isolation involves the insertion of an isolator with appropriate characteristics between the payload and the source of dynamic excitation so that the response is reduced to or controlled at the desired levels. Vibration isolators are commercially available in many forms, for example, rubber, cork, felt, elastomers, damped steel springs, active and semi-active. The stiffness of the supports is chosen to ensure that the natural frequency of the suspension lies far below the range of excitation frequencies.

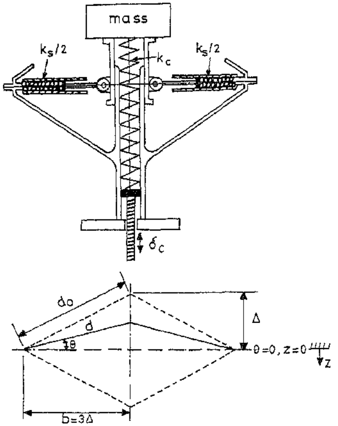

FIG. 1. Proposed constant force device and its geometry

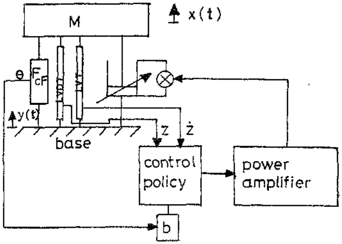

FIG. 2. An sd of model with constant force device and relative control

2. Formulation

Semi-active isolation is a relatively new concept. In the present work, a new semi-active isolation scheme is proposed which uses a constant force device along with semi-active force generator. The objective of the present investigation is to develop a vibration isolator with a very low natural frequency such that the band over which very good isolation is obtained is very large. Low natural frequency is achieved by balancing the static force with a constant force device or a zero spring rate device. A robust design for the constant force device as an assembly of helical compression springs is shown in Fig. 1. The use of constant force device results in high equivalent damping ratios. The vibration isolator modeled as a single degree of freedom system with the constant force device and a semi-active force generator is shown in Fig. 2. The semi-active force generator is a damper that dissipates power depending upon the sign of the condition function. The theory of relative control discussed by Jolly and Miller[1] is applied to the single degree of freedom isolator. The equation of motion from the static equilibrium position ($\theta = 0$) is given by

$$m\ddot{z} + F_{SA} + F_{CF} = -m\ddot{y} \tag{1}$$

$$F_{CF} = k_c \lambda b(\tan\theta - \sin\theta) \tag{2}$$

$$\lambda = (d_0 + \delta_s)/(d_0 + \delta_s - b) \tag{3}$$

where F_{CF} is the force produced by the constant force device, δ_s the precompression of the side spring of stiffness $k_s/2$, and F_{SA} the force of the semi-active damper given by the following equation

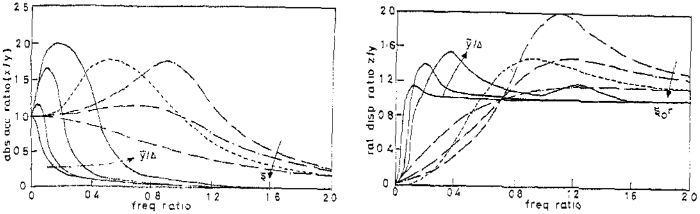

FIG 3. Performance of various types of isolators. — proposed, $\bar{y}/\Delta = 0.1, 0.2, 0.4, 0.8$; ---semi-active linear spring, -·- fully active, $\zeta = 0.3, 0.5, 1.0$

$$\begin{aligned} F_{\mathrm{SA}} &= -\alpha_{\mathrm{d}}\lambda k_c(z - b\theta) + c\dot{z} && \text{if} \quad z\dot{z} \le 0 \\ &= c\dot{z} && \text{if} \quad z\dot{z} > 0 \end{aligned} \tag{4}$$

where α_d is the damper gain. The parameters used in the above equation are shown in Fig. 1. Also the proposed system is inherently stable since no energy is added to the system. The damper only dissipates energy or does nothing at all depending on the sign of the condition function. The term $c\dot{z}$ is the equivalent viscous damping that is always present in the system because of the internal damping and friction at the sliding surfaces.

3. Computations

An algorithm based on directly measurable quantities is developed for the control of forces expected to be generated by the semi-active device. Computer simulation studies of a single degree of freedom model subjected to harmonic base input show that the performance of the proposed scheme is superior to that of both passive and active schemes for low amplitudes of excitation.[2] The response of the isolator is evaluated in terms of shock acceleration ratio and relative displacement ratio for transient inputs of rounded pulse and rounded step displacements. Since the natural time period is very large, the system ignores or does not respond to base inputs lasting for time duration normally encountered in practice.[2]

4. Case studies

The performance of the proposed scheme is studied in four types of multi-degree of freedom systems. In one application, it is shown that the proposed scheme can be used to simulate free flight boundary conditions in ground vibration testing. In the second application, a two-degree of freedom ¼th car model is considered. When the acceleration transmissibility ratios are compared with those from existing schemes, it is seen that the performance of the proposed scheme is superior to that of passive, and hitherto existing semi-active and fully active schemes for low amplitudes of excitation. For large amplitudes of excitation, the performance matches with those from fully active schemes.

The third application is the four-degree-of-freedom half-vehicle model that includes the heave and pitch modes. The absolute acceleration transmissibility ratio at resonance frequency of 0.5 Hz is two for large amplitudes of excitation and for small amplitudes, the resonance peak is close to zero. The secondary suspension travel is equal to the base input displacement for low amplitudes of excitation. The pitch rate is low for small amplitudes of excitation.[2] Even in the fourth application of vibration isolation platform where a three degree of freedom model with heave, pitch and roll modes is studied, it is found that the body accelerations and body rotation rates are low and the suspension travel is equal to the base input. This particular multi-degree of freedom model finds use in stabilisation platforms in aerospace and naval applications and also in automobile suspensions.

5. Conclusion

Using simple, reliable, stable and inexpensive devices, a vibration isolator with a very low natural frequency and superior performance that protects the payload from shock and vibration is developed which is otherwise possible only with complex, unreliable and expensive active systems.

References

1. Jolly, M R and Miller, L. R. The control of semi-active dampers using relative feedback signals, *SAE Trans.* No 892483, pp 569–577.
2. Krishna, Y , Shrinivasa, U. and Sarma, B. S Semi-active vibration isolation using constant force device. Part-I. Steady state analysis, Submitted to SAE, 1998.
3. Krishna, Y., Shrinivasa, U. and Sarma, B. S. Semi-active vibration isolation using constant force device Part-II Transient analysis, Submitted to SAE, 1998.
4. Krishna, Y., Shrinivasa, U. and Sarma, B. S Semi-active vibration isolation using constant force device. Part-III Analysis of a four dof half-vehicle model, Submitted to SAE, 1998